AGU PUBLICATIONS

JGR

Journal of Geophysical Research: Oceans

RESEARCH ARTICLE

10.1002/2013JC009395

Interferometry of infragravity waves off New Zealand

Oleg A. Godin[1,2], Nikolay A. Zabotin[1,3], Anne F. Sheehan[1,4], and John A. Collins[5]

[1]Cooperative Institute for Research in Environmental Sciences, University of Colorado, Boulder, Colorado, USA, [2]Physical Sciences Division, Earth System Research Laboratory, National Oceanic and Atmospheric Administration, Boulder, Colorado, USA, [3]Department of Electrical, Computer, and Energy Engineering, University of Colorado, Boulder, Colorado, USA, [4]Department of Geological Sciences, University of Colorado, Boulder, Colorado, USA, [5]Woods Hole Oceanographic Institution, Woods Hole, Massachusetts, USA

Key Points:
- Background IGWs form a diffuse random anisotropic wavefield off New Zealand
- Compressed cross-correlation function technique enhances wave interferometry
- Interferometry reveals seafloor interaction, spectra, and directionality of IGWs

Correspondence to:
O. A. Godin,
oleg.godin@noaa.gov

Citation:
Godin, O. A., N. A. Zabotin, A. F. Sheehan, and J. A. Collins (2014), Interferometry of infragravity waves off New Zealand, *J. Geophys. Res. Oceans*, *119*, 1103–1122, doi:10.1002/2013JC009395.

Received 31 AUG 2013
Accepted 9 JAN 2014
Accepted article online 15 JAN 2014
Published online 18 FEB 2014

Abstract Wave interferometry is a remote sensing technique, which is increasingly employed in helioseismology, seismology, and acoustics to retrieve parameters of the propagation medium from two-point cross-correlation functions of random wavefields. Here we apply interferometry to yearlong records of seafloor pressure at 28 locations off New Zealand's South Island to investigate propagation and directivity properties of infragravity waves away from shore. A compressed cross-correlation function technique is proposed to make the interferometry of dispersive waves more robust, decrease the necessary noise averaging time, and simplify retrieval of quantitative information from noise cross correlations. The emergence of deterministic wave arrivals from cross correlations of random wavefields is observed up to the maximum range of 692 km between the pressure sensors in the array. Free, linear waves with a strongly anisotropic distribution of power flux density are found to be dominant in the infragravity wavefield. Lowest-frequency components of the infragravity wavefield are largely isotropic. The anisotropy has its maximum in the middle of the spectral band and decreases at the high-frequency end of the spectrum. Highest anisotropy peaks correspond to waves coming from portions of the New Zealand's shoreline. Significant contributions are also observed from waves propagating along the coastline and probably coming from powerful sources in the northeast Pacific. Infragravity wave directivity is markedly different to the east and to the west of the South Island. The northwest coast of the South Island is found to be a net source of the infragravity wave energy.

1. Introduction

Infragravity waves (IGWs) are surface gravity waves in the ocean with periods longer than the longest periods (~30 s) of wind-generated waves. IGWs are believed to be generated by nonlinear interaction of sea swell with bathymetry close to shore [*Foda and Mei*, 1981; *Symonds et al*., 1982; *Herbers et al*., 1995]. Most field observations of IGWs have been made in relatively shallow water on continental shelves [*Munk*, 1949; *Elgar et al*., 1992; *Herbers et al*., 1995; *Sheremet et al*., 2002], where IGWs account for up to half of the wave energy. Deep water IGWs [*Snodgrass et al*., 1966; *Filloux*, 1983; *Webb et al*., 1991], because of their relatively small amplitude of 10^{-3} to 10^{-2} m [*Webb et al*., 1991; *Godin et al*., 2013] and difficulty of access to stable measurement platforms, are among the least studied waves in the ocean. IGW energy balance, directivity, and temporal and spatial variability remain poorly understood [*Dolenc et al*., 2005, 2008; *Sugioka et al*., 2010; *Aucan and Ardhuin*, 2013].

Away from shores, IGWs propagate transoceanic distances with very little attenuation [*Van Dorn*, 1984, 1987; *Geist et al*., 2009; *Rabinovich et al*., 2013] and, because of their long wavelengths (from ~1 km to hundreds of km), provide a mechanism for coupling wave processes in the ocean, ice shelves, the atmosphere, and the solid Earth [*Peltier and Hines*, 1976; *Crawford et al*., 1998; *Rhie and Romanowicz*, 2004; *Bromirski et al*., 2010; *Godin and Fuks*, 2012; *Bromirski and Stephen*, 2012; *Ardhuin and Herbers*, 2013]. In polar seas, long IGWs penetrate thousands of kilometers inside the ice cover and can be used to measure sea ice thickness [*Squire et al*., 2009; *Wadhams and Doble*, 2009]. The strong response of ice shelves to impacting IGWs suggests that IGW forcing may produce fractures in the ice and lead to abrupt disintegration of ice shelves [*Bromirski et al*., 2010; *Bromirski and Stephen*, 2012]. In seismology, IGWs are one of the dominant noise sources that limit performance and restrict the useful frequency band of ocean bottom seismometers [*Webb*, 1998; *Webb and Crawford*, 2010]. IGWs are responsible for generation of the Earth's "hum," i.e., persistent

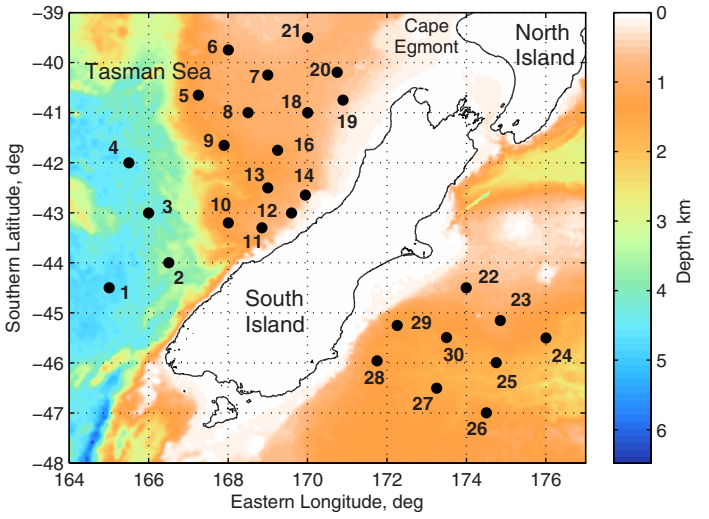

Figure 1. Bathymetry map and location of seafloor pressure sensors, which are shown by numbered circles, in the MOANA experiment.

excitation of the seismic normal modes of the Earth [*Rhie and Romanowicz*, 2004; *Tanimoto*, 2005; *Ardhuin and Herbers*, 2013]. IGWs provide the signal to probe the shear rigidity deep into the ocean bottom via seafloor compliance measurements [*Crawford*, 2004; *Crawford and Singh*, 2008; *Crawford et al*., 1991, 1998; *Trevorrow and Yamamoto*, 1991; *Wang et al*., 2010; *Willoughby and Edwards*, 2000; *Willoughby et al*., 2008]. At frequencies below ∼4 mHz, IGWs are an effective mechanism for transporting mechanical energy from the ocean into the upper atmosphere [*Livneh et al*., 2007; *Makela et al*., 2011; *Galvan et al*., 2012; *Godin and Fuks*, 2012]. Ambient IGWs contribute to the background "noise" level against which tsunamis need to be detected in deep water. The need for a global IGW model to determine the waves' impact on future high-resolution satellite altimetry missions has been recently demonstrated [*Aucan and Ardhuin*, 2013].

Hydrodynamic filtering, i.e., attenuation of surface waves with depth on the scale of their wavelength, reverses the relation of amplitudes of short-period and long-period surface gravity waves at large depths. IGWs dominate seafloor pressure fluctuations in deep water from frequencies from a fraction of mHz to as much as tens of mHz [*Filloux*, 1983; *Webb*, 1986, 1988; *Webb et al*., 1991]. Most of the current knowledge about IGWs away from shore stems from the data obtained using pressure sensors and seismometers located on the seafloor [*Filloux*, 1983; *Webb*, 1986; *Webb et al*., 1991; *Crawford et al*., 1991; *Dolenc et al*., 2005, 2008; *Sugioka et al*., 2010; *Harmon et al*., 2012; *Yang et al*., 2012; *Aucan and Ardhuin*, 2013].

The present work is based on an analysis of long, continuous time series of seafloor pressure variations collected concurrently at 28 deep water locations off the South Island of New Zealand (Figure 1) during the MOANA seismic experiment [*Yang et al*., 2012; *Godin et al*., 2013]. Variances of seafloor pressure fluctuations observed in this experiment have been recently used to derive an analytical model of the spectral and spatial energy distribution of IGW energy in a deep ocean with variable bathymetry [*Godin et al*., 2013]. Here we investigate the information content of two-point statistical moments (specifically, of the mutual correlation functions) of seafloor pressure fluctuations measured in deep water at locations tens and hundreds kilometers apart.

Wavefields generated by random, delta-correlated sources are known to remain partially coherent at points separated by distances that are large compared to the wavelength [*Weaver and Lobkis*, 2001; *Campillo and Paul*, 2003; *Shapiro et al*., 2005; *Wapenaar et al*., 2008]. Two-point cross-correlation functions of diffuse (i.e., having at each observation point components with a wide variety of propagation directions), random wavefields have been shown to approximate the Green's functions, which describe deterministic wave propagation between the two points [*Rytov*, 1956; *Lobkis and Weaver*, 2001; *Snieder*, 2004; *Godin*, 2006, 2009a; *Gouédard et al*., 2008]. Hence, observation of waves generated by controlled sources can be replaced by cross correlation of ambient random wavefields, which would be classified as noise in active-source experiments. This passive technique is usually referred to as wave, seismic, or noise interferometry. It is extensively used in helioseismology, seismology, and acoustics to retrieve parameters of the propagation medium from cross-correlation functions of random wavefields [*Duvall et al*., 1993; *Rickett and Claerbout*, 1999; *Shapiro et al*., 2005; *Larose et al*., 2006; *Wapenaar et al*., 2008; *Godin et al*., 2010].

In IGW context, *Webb* [1986] was the first to study long-range correlations of seafloor pressure fluctuations in deep water. He measured coherence in the frequency band 1–15 mHz of pressure fluctuations at points 32 km apart in 4.2 km-deep water off Baja California and found the result to be consistent with a weakly

anisotropic, diffuse field of IGWs [*Webb*, 1986]. Cross correlations of seafloor pressure fluctuations over an 80 km × 80 km area off California in 5.1 km-deep water were used to measure IGW directivity at frequencies above 2 mHz with an 11 element array [*Webb et al*., 1991]. Dominant source regions of IGWs in the ~5 to 15 mHz frequency band were investigated using cross correlations of seafloor pressure recorded off Sumatra at five points ~30 to ~130 km apart from each other [*Harmon et al*., 2012]. In the present work, noise interferometry is applied to a much larger array with distances from ~50 to ~700 km between individual seafloor pressure sensors, to reveal information about an ambient, deep water IGW field over complex bathymetry in the frequency band 0.5–30 mHz.

The remainder of this paper is organized as follows. In section 2, having formulated the problem in mathematical terms (section 2.1), we provide a theoretical background for interferometric processing and interpretation of seafloor pressure observations by developing an asymptotic theory of IGW fields due to deterministic and random sources in a three dimensionally inhomogeneous ocean (section 2.2). Motivated by theoretical predictions of the properties of the IGW cross correlations, we propose a novel interferometric technique based on compressed cross-correlation functions (section 2.3). Seafloor pressure data obtained in the MOANA experiment and the data-processing algorithms we used to implement the compressed cross-correlation function technique, including a self-calibration of the pressure sensors, are described in section 3. Experimental results are presented in section 4. Additional oceanographic opportunities offered by the IGW interferometry are discussed in section 5. Section 6 summarizes our findings.

2. Theory

In this section, we establish a method for retrieval of quantitative information regarding power fluxes carried by IGWs from seafloor pressure fluctuations measured at several locations in a three dimensionally inhomogeneous ocean. We also devise a method to compensate for IGW dispersion and accelerate the emergence of deterministic features from cross correlations of random pressure fluctuations. These methods form the basis for our data processing.

2.1. Governing Equations

Introduce a Cartesian coordinate system with horizontal coordinates x and y and the vertical coordinate z increasing downward, i.e., in the direction of the gravity acceleration $\mathbf{g}$. The fluid is motionless in the absence of waves and occupies a layer $0 < z < H$ between a free boundary at $z = 0$ and seafloor at $z = H(x, y)$. Denote p_0, p, and $\mathbf{w}$ the background pressure (i.e., the pressure in fluid in the absence of waves), wave-induced pressure perturbation at a given point, and wave-induced displacement of fluid particles, respectively. The displacement and fluid velocity $\mathbf{v}$ are related by $\mathbf{v}=\partial\mathbf{w}/\partial t$, where t is time. Linearization of the Euler, continuity, and state equations with respect to wave amplitude leads to the following set of equations governing linear (i.e., small amplitude) wavefields [*Gill*, 1982; *Brekhovskikh and Godin*, 1999]:

$$\rho c^2\left[\nabla p+\rho\partial^2\mathbf{w}/\partial t^2+(\mathbf{w}\cdot\nabla)\nabla p_0\right]-(p+\mathbf{w}\cdot\nabla p_0)\nabla p_0=0, \tag{1}$$

$$p+\mathbf{w}\cdot\nabla p_0+\rho c^2\nabla\cdot\mathbf{w}=0, \tag{2}$$

where $\nabla p_0=\rho\mathbf{g}$ and c is the sound speed. The boundary conditions on the free surface and the rigid seafloor are [e.g., *Gill*, 1982; *Brekhovskikh and Godin*, 1999] $p=\rho g w_3$ at $z = 0$ and $w_3=\mathbf{w}\cdot\nabla H$ at $z = H$.

Consider waves with the harmonic dependence $\exp(i\mathbf{k}\cdot\mathbf{r}-i\omega t)$, where $\mathbf{k} = (k_1, k_2, 0) = \text{const.}$, on horizontal coordinates and time in an ocean of constant depth. Most investigations of IGWs imply an incompressible ocean with constant water density and a rigid seafloor [*Webb*, 1986; *Webb et al*., 1991; *Thomson et al*., 2007; *Harmon et al*., 2012]. Under these assumptions, the vertical dependences of pressure and particle displacement in surface gravity waves are

$$p(z)=p(0)\frac{\cosh k(H-z)}{\cosh kH},\ w_3(z)=-\frac{p(0)}{\rho g}\frac{\sinh k(H-z)}{\sinh kH}, \tag{3}$$

and IGWs have the dispersion equation [e.g., *Eckart*, 1960; *Gill*, 1982]:

$$\omega^2 = gk \tanh kH. \tag{4}$$

The group speed is

$$c_g = \left(\frac{\partial\omega}{\partial k}\right)_H = \frac{\omega}{k}\cdot\frac{2kH+\sinh 2kH}{2\sinh 2kH}. \tag{5}$$

Except in shallow water with depth $H << g\omega^{-2}$, IGWs are strongly dispersive. At constant depth, the phase speed $c_{ph} = \omega/k$, the group speed c_g, and the ratio c_g/c_{ph} steadily decrease with frequency from the frequency-independent "shallow-water" values $(gH)^{1/2}$, $(gH)^{1/2}$, and 1 at $\omega << (gH)^{1/2}$ to the depth-independent "deep water" values g/ω, $g/2\omega$, and 0.5 at $\omega >> (gH)^{1/2}$.

2.2. Deterministic and Random IGWs in a Horizontally Inhomogeneous Ocean

Spatial variations of bathymetry and other physical parameters of the ocean cause refraction, focusing, and defocusing of IGWs. To reveal the relation between IGW power fluxes and observed pressure fluctuations, we first briefly consider asymptotics of the field due to a point source and then represent the diffuse IGW field as a superposition of fields due to random point sources. Amplitudes of the peaks of the cross-correlation function prove to be directly related to the power flux carried by IGWs.

2.2.1. Point-Source Excitation

Consider an ocean where physical parameters, including the ocean depth, vary gradually in the horizontal plane. The spatial scale of the horizontal variations is assumed to be large compared to the IGW wavelength. The ocean is stationary in the absence of waves. Let acoustic-gravity waves be generated by a monochromatic point source of mass with the amplitude a_0 of the volume injection rate. Such a source is described mathematically by adding the term $(-i\omega)^{-1}a_0\rho c^2\delta(\mathbf{R}-\mathbf{R}_1)$ in the right-hand side of equation (2) [*Brekhovskikh and Godin*, 1999], where $\delta(\cdot)$ is the Dirac delta function, $\mathbf{R} = (x, y, z)$, and $\mathbf{R}_1 = (x_1, y_1, z_1)$ is the location of the wave source. In the adiabatic approximation, the field of a normal mode excited by the point source in a horizontally inhomogeneous waveguide is [*Keller*, 1958; *Weinberg and Burridge*, 1974; *Shen and Keller*, 1975; *Brekhovskikh and Godin*, 1999]

$$p(\mathbf{R},\omega) = i\omega a_0 P(z;\mathbf{r})P(z_1;\mathbf{r}_1)G(\mathbf{r},\mathbf{r}_1), \tag{6}$$

where $\mathbf{r} = (x, y)$ and $\mathbf{r}_1 = (x_1, y_1)$ are 2-D horizontal vectors and the function G satisfies the 2-D Helmholtz equation

$$\partial^2 G(\mathbf{r},\mathbf{r}_1)/\partial\mathbf{r}^2 + k^2(\mathbf{r})G(\mathbf{r},\mathbf{r}_1) = \delta(\mathbf{r}-\mathbf{r}_1) \tag{7}$$

with radiation conditions at $|\mathbf{r}-\mathbf{r}_1| \to \infty$. Here $P(z;\mathbf{r})$ and $k(\mathbf{r})$ and the mode shape function (i.e., the vertical profile of pressure) and the mode wave number in an auxiliary, horizontally homogeneous waveguide having the same depth, seafloor compliance, and sound speed and density profiles that the original, horizontally inhomogeneous waveguide has at the given x and y. When IGW dissipation and possible radiation into the atmosphere are neglected, Im $k(\mathbf{r}) = 0$. In a waveguide with a free surface at $z = 0$ and a rigid seafloor at $z = H$, the mode shape functions in equations (6) and (7) are normalized by the condition

$$\int_0^{H(\mathbf{r})} \rho^{-1}(z;\mathbf{r})P^2(z;\mathbf{r})dz = 1 \tag{8}$$

and are real valued.

The function G can be viewed as the Green's function of the 2-D Helmholtz equation (7), i.e., the field due to a unit point source in the 2-D problem in the horizontal plane. It satisfies the reciprocity relation $G(\mathbf{R}, \mathbf{R}_1) = G(\mathbf{R}_1, \mathbf{R})$ and, when Im $k(\mathbf{r}) = 0$, the identity [e.g., *Larose et al.*, 2006]

$$G(\mathbf{r}_2,\mathbf{r}_1)-G^*(\mathbf{r}_2,\mathbf{r}_1)=\oint\mathbf{N}(\mathbf{r})\cdot\left[G(\mathbf{r},\mathbf{r}_1)\frac{\partial}{\partial\mathbf{r}}G^*(\mathbf{r},\mathbf{r}_2)-G^*(\mathbf{r},\mathbf{r}_2)\frac{\partial}{\partial\mathbf{r}}G(\mathbf{r},\mathbf{r}_1)\right]d\mathbf{r}, \tag{9}$$

which follows from equation (7). Here and below, the asterisk denotes complex conjugation. Integration in equation (9) is over the boundary of an arbitrary domain containing points $\mathbf{r}_1$ and $\mathbf{r}_2$; $\mathbf{N}$ is the unit external normal to the boundary.

An asymptotic solution for $G(\mathbf{R}, \mathbf{R}_1)$ can be found in the ray, or geometric optics, approximation [*Keller*, 1958; *Weinberg and Burridge*, 1974; *Shen and Keller*, 1975; *Brekhovskikh and Godin*, 1999]. In this approximation, normal modes propagate from the wave source along horizontal trajectories (rays). The position of a point $\mathbf{r}(l, \varphi)$ on a horizontal ray and the mode wave vector $\mathbf{k}(l, \varphi) = (k_x, k_y)$ at this point are found from the differential ray equations

$$d\mathbf{r}/dl=\mathbf{k}/k,\quad d\mathbf{k}/dl=\partial k/\partial\mathbf{r}, \tag{10}$$

where l and φ are the arc length along the ray and the azimuthal angle giving the direction of the ray at the source. For a generic dependence of the ocean depth on horizontal coordinates, equations (10) have to be integrated numerically. In the ray approximation,

$$G(\mathbf{r},\mathbf{r}_1)=\frac{\exp\left(i\Phi(\mathbf{r},\mathbf{r}_1)-3i\pi/4\right)}{\sqrt{8\pi\left[k_x(\partial y/\partial\varphi)_l-k_y(\partial x/\partial\varphi)_l\right]}},\quad \Phi(\mathbf{r},\mathbf{r}_1)=\int_{\mathbf{r}_1}^{\mathbf{r}}kdl. \tag{11}$$

Integration in the exponential in equation (11) is along an eigenray, i.e., the horizontal ray that connects points $\mathbf{r}_1$ and $\mathbf{r}$. In a horizontally homogeneous ocean, $\partial k/\partial\mathbf{r}=0$, horizontal rays are straight lines, $x=x_1+l\cos\varphi, y=y_1+l\sin\varphi$, and equation (11) simplifies to $G(\mathbf{r},\mathbf{r}_1)=(8\pi k|\mathbf{r}-\mathbf{r}_1|)^{-1/2}\exp\left(ik|\mathbf{r}-\mathbf{r}_1|-3i\pi/4\right)$, which coincides with the dominant term of the asymptotic expansion at $k|\mathbf{r}-\mathbf{r}_1|\to\infty$ of the exact solution $G(\mathbf{r},\mathbf{r}_1)=H_0^{(1)}(k|\mathbf{r}-\mathbf{r}_1|)/4i$ of equation (7).

2.2.2. Excitation by Random Sources

Let Ω be a simply connected area on the horizontal plane with a smooth boundary $\partial\Omega$, and let monochromatic wave sources be located on a cylindrical surface $\{\mathbf{r}\in\partial\Omega, 0\le z\le H\}$. The curve $\partial\Omega$ is parameterized by its arc length l; for every point $\mathbf{r}\in\partial\Omega$, we have $\mathbf{r}=\mathbf{r}_\Omega(l)$. The sources are characterized by the density $a(l, z)$ of the volume injection rate they generate. As with the mode shape function P and the 2-D Green's function G, dependence of the source strength on frequency ω is assumed and suppressed. For the IGW field generated by a distributed source, from equation (6) we find

$$p(\mathbf{R},\omega)=i\omega P(z;\mathbf{r})\int_{\partial\Omega}dl\int_0^{H(\mathbf{r}_\Omega(l))}a(l,z_1)P(z_1;\mathbf{r}_\Omega(l))G(\mathbf{r},\mathbf{r}_\Omega(l))dz_1. \tag{12}$$

Consider random wave sources with zero statistical mean: $<a> = 0$. At each point, a is a stationary random process. In the time domain, the wavefield is random and stationary as well, and $<p(\mathbf{R})> = 0$. Let the wave sources be δ-correlated in the horizontal plane:

$$\langle a(l_1,z_1,\omega)a^*(l_2,z_2,\omega')\rangle=A(z_1,z_2,l_1,\omega)\delta(l_1-l_2)\delta(\omega-\omega'). \tag{13}$$

No assumptions about correlation in the vertical direction are made; δ-correlation in frequency reflects the assumption that the sources are stationary in time. As its particular cases, the model includes IGW generation by sources on the ocean surface or on the seafloor. Using equations (12) and (13), for the frequency-domain cross-correlation function (or cross spectrum) $C(\mathbf{R}_1,\mathbf{R}_2,\omega)=\langle p(\mathbf{R}_1,\omega)p^*(\mathbf{R}_2,\omega)\rangle$ of the pressure measured at points $\mathbf{R}_1$ and $\mathbf{R}_2$, we find

$$C(\mathbf{R}_1,\mathbf{R}_2,\omega)=P(z_1;\mathbf{r}_1)P(z_2;\mathbf{r}_2)C_1(\mathbf{r}_1,\mathbf{r}_2,\omega), \tag{14}$$

$$C_1(\mathbf{r}_1,\mathbf{r}_2,\omega)=\int_{\partial\Omega}Q(l)G(\mathbf{r}_1,\mathbf{r}_\Omega(l))G^*(\mathbf{r}_2,\mathbf{r}_\Omega(l))dl, \tag{15}$$

where

$$Q(l)=\omega^2\int_0^{H(\mathbf{r}_\Omega(l))}\int_0^{H(\mathbf{r}_\Omega(l))}A(z_3,z_4,l,\omega)P(z_3;\mathbf{r}_\Omega(l))P(z_4;\mathbf{r}_\Omega(l))dz_3dz_4. \quad (16)$$

The factor C_1 in equation (14) for the cross-correlation function coincides with the cross-correlation function of noise generated by δ-correlated sources in a 2-D problem. The latter problem has been solved in the acoustical context [*Godin*, 2006, 2010]. In the ray approximation,

$$C_1(\mathbf{r}_1,\mathbf{r}_2,\omega)=i\tilde{Q}_1G(\mathbf{r}_1,\mathbf{r}_2)+i\tilde{Q}_2G^*(\mathbf{r}_1,\mathbf{r}_2),\quad \tilde{Q}_j=\frac{Q(l_j)}{2\mathbf{k}(\mathbf{r}_\Omega(l_j))\cdot\mathbf{N}(l_j)},j=1,2, \quad (17)$$

provided there exists exactly one horizontal eigenray connecting points $\mathbf{r}_1$ and $\mathbf{r}_2$. Here $\mathbf{r}_\Omega(l_j)$ are the points, where extensions of the eigenray intersect the curve $\partial\Omega$, and $\mathbf{k}(\mathbf{r})$ is the wave vector on this ray. In a more general situation, where there are M eigenrays connecting points $\mathbf{r}_1$ and $\mathbf{r}_2$, equation (17) becomes

$$C_1(\mathbf{r}_1,\mathbf{r}_2,\omega)=\sum_{m=1}^{M}\left[S_{1m}e^{i\Phi_m(\mathbf{r}_1,\mathbf{r}_2,\omega)-i\pi/4}+S_{2m}e^{-i\Phi_m(\mathbf{r}_1,\mathbf{r}_2,\omega)+i\pi/4}\right]. \quad (18)$$

Here $\Phi_m(\mathbf{r}_1,\mathbf{r}_2,\omega)\geq 0$ is the increment of the eikonal (phase) between points $\mathbf{r}_1$ and $\mathbf{r}_2$ calculated along the mth eigenray. (Phase corrections at caustics are to be included in the eikonal.) Equation (18) differs from the ray approximation to $\mathrm{Im}\,G(\mathbf{r}_1,\mathbf{r}_2)$ by the real-valued amplitudes S_{1m} and S_{2m} of the individual ray contributions. The amplitudes are proportional to the values of the effective source density Q (16) at the points, where extension of the mth eigenray intersects $\partial\Omega$. S_{1m} and S_{2m} are given by the product of corresponding factor $\tilde{Q}_j$ (17) and the ray amplitude at propagation from a unit point source at $\mathbf{r}_1$ to a receiver at $\mathbf{r}_2$. The latter factor may depend on m but is common for S_{1m} and S_{2m}.

The results (14), (17), and (18) are considerably more general than the assumptions we made in their derivation. When waves are generated by random sources other than the sources of mass, e.g., by sources of an external force, only the expression (16) for the density of the effective sources changes [*Godin*, 2009a, 2010]. Equation (18) remains valid for arbitrary located noise sources as long as wave dissipation and contributions of sources within the domain Ω are negligible [*Godin*, 2010]. Then, the amplitude factor $\tilde{Q}_j$ (17) includes weighted contributions of the noise sources located in the vicinity of the extensions of the respective eigenray beyond the points $\mathbf{r}_1$ and $\mathbf{r}_2$. Explicit expressions for the amplitudes can be found in *Godin* [2010]. The assumption of the random sources being δ-correlated in the horizontal plane also can be relaxed and replaced by the condition that their correlation length is small compared to the size of the Fresnel zone at wave propagation between points $\mathbf{r}_1$ and $\mathbf{r}_2$ [*Godin*, 2009b].

Through the eikonals $\Phi_m(\mathbf{r}_1,\mathbf{r}_2,\omega)$, the noise cross-correlation function C (14), (18) contains information about the wave dispersion relation and deterministic properties of the propagation medium. Information about the frequency spectra and spatial distribution of the random wave sources is contained in the amplitude factors S_{1m} and S_{2m}. Let us demonstrate that the ratio S_{1m}/S_{2m} provides a direct measure of the noise field anisotropy.

Power flux density in continuous acoustic-gravity waves $\mathbf{j}=\omega\mathrm{Im}\,(p^*\mathbf{w})$ [*Brekhovskikh and Godin*, 1999]. From equations (1), (2), (6), and (8), for the depth-integrated horizontal power flux in a single normal mode generated by a point source, we have

$$\mathbf{j}_h(\mathbf{r},\omega)=\int\mathbf{j}(\mathbf{R},\omega)dz=\omega|a_0^2|\mathrm{Im}\,[G^*(\mathbf{r},\mathbf{r}_1)\partial G(\mathbf{r},\mathbf{r}_1)/\partial\mathbf{r}]. \quad (19)$$

For a distribution of random wave sources δ-correlated in the horizontal plane, using equations (12) and (13) we find

$$\langle\mathbf{j}_h(\mathbf{r},\omega)\rangle=\omega\int_{\partial\Omega}Q(l)\mathrm{Im}\,[G^*(\mathbf{r},\mathbf{r}_\Omega(l))\partial G(\mathbf{r},\mathbf{r}_\Omega(l))/\partial\mathbf{r}]dl. \quad (20)$$

Note the similarity between the right-hand sides of equation (20) for the average power flux and equation (15) for the two-point cross-correlation function of the random wavefield.

In the adiabatic approximation,

$$\partial G(\mathbf{r}, \mathbf{r}_\Omega(I))/\partial \mathbf{r} = i\mathbf{k}(\mathbf{r}, I) G(\mathbf{r}, \mathbf{r}_\Omega(I)), \mathbf{k}(\mathbf{r}, I) = k(\mathbf{r})(\cos\varphi(\mathbf{r}, I), \sin\varphi(\mathbf{r}, I), 0), \tag{21}$$

where the azimuthal angle $\varphi(\mathbf{r}, I)$ describes the direction of the wave vector and the power flux at point $\mathbf{r}$. Here we assume that there exists only one horizontal eigenray connecting points $\mathbf{r}$ and $\mathbf{r}_\Omega(I)$. Waves with different values of φ originate at different points on $\partial\Omega$, so that $I = I(\varphi)$. It follows from equation (20) that the average power flux per unit azimuthal angle per unit frequency in the direction φ is

$$J(\mathbf{r}, \varphi, \omega) = \omega Q(I) k(\mathbf{r}) |G(\mathbf{r}, \mathbf{r}_\Omega(I))|^2 |dI/d\varphi|. \tag{22}$$

The average power flux density characterizes the intensity and directivity of the random wavefield.

To simplify equation (22), we use wave reciprocity and reversibility of rays. Consider the horizontal ray leaving the observation point $\mathbf{r}$ in the direction $\varphi - \pi$. The ray is given by an equation $\mathbf{r}(s, \varphi)$, where s is the arc length along the ray, and intersects $\partial\Omega$ at some point $\mathbf{r}_\Omega(I(\varphi))$. Using the differential ray equations (10), one finds

$$\frac{dI}{d\varphi} = \pm\left|\frac{d\mathbf{r}_\Omega}{d\varphi}\right| = \pm\frac{1}{\mathbf{k}\cdot\mathbf{N}}\left|\mathbf{k}\times\left(\frac{\partial\mathbf{r}}{\partial\varphi}\right)_s\right|, \tag{23}$$

where $\mathbf{N}$ is the unit external normal to $\partial\Omega$, as in equations (9) and (17), and the values of $\mathbf{k}$ and $(\partial\mathbf{r}/\partial\varphi)_s$ on the ray are evaluated at the point of its intersection with $\partial\Omega$. Since $|G(\mathbf{r}, \mathbf{r}_\Omega(I))|^2 = |G(\mathbf{r}_\Omega(I), \mathbf{r})|^2 = (8\pi|\mathbf{k}\times(\partial\mathbf{r}/\partial\varphi)_s|)^{-1}$ according to equation (11), from equations (22) and (23) one finds

$$J(\mathbf{r}, \varphi, \omega)/k(\mathbf{r}) = \omega Q(I)/8\pi|\mathbf{k}(\mathbf{r}_\Omega(I))\cdot\mathbf{N}(I)|. \tag{24}$$

Thus, the quantity J/k, i.e., the ratio of the power flux density along a ray divided by the local value of the wave number, remains constant in Ω on any horizontal ray. Comparison of equations (17) and (24) shows that the ratio of power fluxes carried in opposite directions along an eigenray connecting two observation points is equal to the ratio of the amplitude factors $\tilde{Q}_1$ and $\tilde{Q}_2$ in the noise cross-correlation function and can be readily measured by the noise interferometry technique. Note that, although only a fraction of the waves comprising the diffuse wavefield is correlated, the ratio of the amplitude factors $\tilde{Q}_1$ and $\tilde{Q}_2$ characterizes the net power fluxes in the entire diffuse field in opposite directions along the eigenray. A similar result was reported recently for waves in a homogeneous medium [*Wapenaar and Thorbecke*, 2013].

2.3. Compressed Cross-Correlation Function

In this section, we use results of section 2.2 to develop a technique for robust retrieval of the amplitude and directivity information from measured cross-correlation functions of diffuse fields of dispersive waves.

For stationary random wave sources, the cross-correlation function in the time domain, $C(\mathbf{R}_1, \mathbf{R}_2, \tau) = \langle p(\mathbf{R}_1, t) p(\mathbf{R}_2, t-\tau)\rangle$, is related to the cross spectrum $C(\mathbf{R}_1, \mathbf{R}_2, \omega)$ we considered in section 2.2 by the equation

$$C(\mathbf{R}_1, \mathbf{R}_2, \tau) = 2\mathrm{Re}\int_0^\infty C(\mathbf{R}_1, \mathbf{R}_2, \omega)\exp(-i\omega\tau)d\omega, \tag{25}$$

which follows from equation (13). For nondispersive waves, such as underwater sound, the cross-correlation function of broadband diffuse noise has well defined, robust peaks, which allow one to passively measure deterministic travel times with high accuracy and characterize the environment [*Roux et al.*, 2004; *Godin et al.*, 2010; *Lani et al.*, 2013]. When the correlation function is estimated using time series of finite duration, there occur random deviations of the finite-time estimates of the correlation function from its true value. With the travel times of various frequency components being the same, random deviations of the estimates

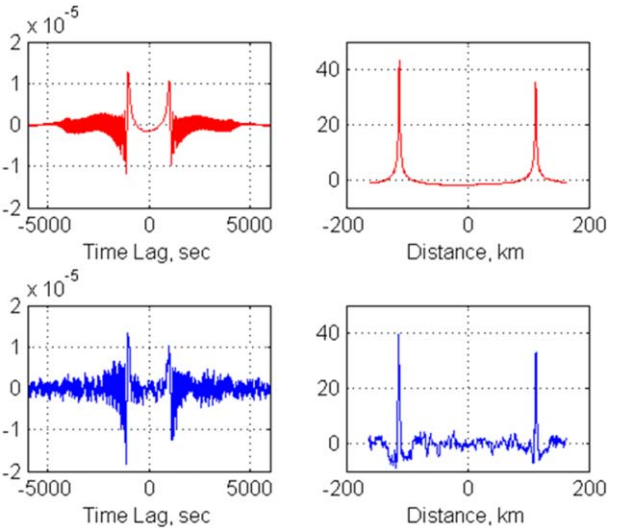

Figure 2. Simulation results (red plots) and results of data processing (blue plots) for stations 24–25 separated by 112.4 km distance. Cross-correlation functions are shown in the left column; compressed cross-correlation functions, or C3Fs, are shown in the right column. Peaks in C3Fs are located at distances ±112.4 km, which coincide with the station separation distance.

of $C(\mathbf{R}_1, \mathbf{R}_2, \tau)$ in various frequency subbands tend to cancel each other, leading to a rapid decrease in the necessary averaging time with increasing frequency band [*Weaver and Lobkis*, 2005; *Sabra et al*., 2005; *Gouédard et al*., 2008; *Zabotin and Godin*, 2011]. This cannot be expected for strongly dispersive waves, such as IGWs, because deterministic travel times vary with frequency. As illustrated in Figure 2, the cross-correlation function of IGWs measured at two distant locations contains numerous peaks and troughs in the time domain, which are not well suited for retrieval of environmental information and are liable to be distorted by instrument noise, errors due to finite averaging time, etc. The simulations presented in Figure 2 are based on equations (17) and (25) assuming constant ocean depth $H = 1600$ m, slight anisotropy of the IGW field: $\tilde{Q}_2/\tilde{Q}_1 = 9/11$, and an IGW power spectrum that is flat between 0.5 and 30 mHz.

To overcome the difficulties associated with the wave dispersion, we introduce a new object

$$C_{12}^{(c)}(L) = 2\mathrm{Re}\int_0^\infty H_{12}(\omega)\exp\left(i\left[\Phi(\mathbf{r}_1, \mathbf{r}_2, \omega) - \frac{\pi\gamma}{4}\right]\frac{L}{L_0}\right)d\omega \tag{26}$$

to be referred to as compressed cross-correlation function (C3F). Here $H_{12}(\omega) = \langle p(\mathbf{R}_1, \omega)p^*(\mathbf{R}_2, \omega)/|p(\mathbf{R}_1, \omega)p^*(\mathbf{R}_2, \omega)|\rangle$ is the coherence function of the observations made at points $\mathbf{R}_1$ and $\mathbf{R}_2$; $\Phi(\mathbf{r}_1, \mathbf{r}_2, \omega)$ is the eikonal increment on an eigenray connecting the observation points; L is a new independent variable with dimensionality of length; and L_0 is a normalization constant, which we choose to be equal to the horizontal separation $|\mathbf{r}_2 - \mathbf{r}_1|$ of the points $\mathbf{R}_1$ and $\mathbf{R}_2$. The constant γ in equation (26) is chosen depending on the type of the eigenray considered and reflects the relation between the eikonal Φ and the phase of the corresponding ray contribution to the deterministic Green's function. For surface waves, $\gamma = 1$ for eigenrays that do not touch any, or have an even number of contacts with, caustics between points $\mathbf{r}_1$ and $\mathbf{r}_2$, see equations (11) and (17); $\gamma = 3$ for eigenrays that have an odd number of contacts with caustics. For body waves, $\gamma = 0$ ($\gamma = 2$) for the eigenrays with an even (odd) number of contacts with their caustics.

We use the coherence function H_{12} rather than the cross spectrum $C(\mathbf{R}_1, \mathbf{R}_2, \omega)$ in the definition (26) of C3F to suppress the effects of a rapid variation of the IGW power spectrum with frequency. The coherence function can be viewed as the cross spectrum of two random fields, the power spectra of which are prewhitened in each realization. When statistical (ensemble) averages are estimated as averages over a large number of time windows of finite duration, the implied prewhitening should be performed in each window. This procedure can be viewed as a frequency-domain counterpart of the "one-bit correlation" in the time domain [*Larose et al*., 2006], which is extensively utilized in noise interferometry.

It follows from equation (18) that, when there is only one eigenray connecting the observation points, the compressed cross-correlation function (26) "compresses" all the peaks that the correlation function $C(\mathbf{R}_1, \mathbf{R}_2, \tau)$ of IGWs has at various positive (negative) τ to a single peak at negative (positive) L (Figure 2). The peaks of C3F are located at $\pm L_0$. For nondispersive waves and white noise, the cross-correlation function (25) and C3F (26) are essentially identical in the absence of caustics: $C_{12}^{(c)}(L) = E^{-1}C\left(\mathbf{R}_1, \mathbf{R}_2, -LL_0^{-1}\partial\Phi/\partial\omega\right)$. Here $\partial\Phi/\partial\omega$ and $E = (\langle|p^2(\mathbf{R}_1, \omega)|\rangle\langle|p^2(\mathbf{R}_2, \omega)|\rangle)^{1/2}$ are independent of frequency.

In the particular case of a horizontally homogeneous ocean, $\Phi(\mathbf{r}_1, \mathbf{r}_2, \omega) = k(\omega)L_0$, the coherence function of diffuse noise $H_{1,2}(\omega) = h_1(\omega)\exp[ik(\omega)L_0 - i\pi/4] + h_2(\omega)\exp[-ik(\omega)L_0 + i\pi/4]$, and the definition (26) of C3F gives

$$C_{12}^{(c)}(L) = 2\mathrm{Re}\int_0^\infty \left\{h_1 e^{-ik(\omega)(L-L_0)} + h_2 e^{-ik(\omega)(L+L_0)}\right\} d\omega = \int_{-\infty}^{\infty} \left[h_1 e^{-ik(L-L_0)} + h_2 e^{-ik(L+L_0)}\right] c_g dk, \tag{27}$$

where c_g is the group speed. The amplitude factors $h_{1,2}(\omega)$ in equation (27) can be viewed as slowly varying functions of frequency as long as L_0 is sufficiently large. Recalling the identity $\delta(x) = (2\pi)^{-1}\int_{-\infty}^{\infty} e^{ikx} dk$, it is clear that the compressed cross-correlation function (27) approximates a linear combination of delta functions $\delta(L - L_0)$ and $\delta(L + L_0)$. The actual width of peaks around $L = L_0$ and $L = -L_0$ is determined by the frequency band, in which the coherence function is measured, and the rate of variation of $h_{1,2}$ and k with frequency.

If the wavefield is due to a point source located at a point $\mathbf{R}_3 = (\mathbf{r}_3, z_3)$, the coherence function is proportional to $\exp[ik(\omega)L_3]$, where $L_3 = |\mathbf{r}_1 - \mathbf{r}_3| - |\mathbf{r}_2 - \mathbf{r}_3|$. Then, instead of two peaks at $L = \pm L_0$, the compressed cross-correlation function will have a single peak at $L \approx L_3$ provided $kL_0 >> 1$. Note that $|L_3| \le L_0$; $|L_3| = L_0$ only when $\mathbf{r}_3$ belongs to the line through $\mathbf{r}_1$ and $\mathbf{r}_2$. Hence, by calculating C3F for two or more pairs of receivers, one can distinguish between diffuse wavefields and fields due to a compact source. This conclusion holds also for a horizontally inhomogeneous ocean since the eikonals for eigenrays that connect points $\mathbf{r}_1$, $\mathbf{r}_2$, and $\mathbf{r}_3$ satisfy an inequality similar to the geometric inequality $|L_3| \le L_0$ utilized in the above reasoning. Indeed, $|\Phi(\mathbf{r}_1, \mathbf{r}_3, \omega) - \Phi(\mathbf{r}_2, \mathbf{r}_3, \omega)| \le \Phi(\mathbf{r}_1, \mathbf{r}_2, \omega)$ according to Fermat's principle, and $|\Phi(\mathbf{r}_1, \mathbf{r}_3, \omega) - \Phi(\mathbf{r}_2, \mathbf{r}_3, \omega)| = \Phi(\mathbf{r}_1, \mathbf{r}_2, \omega)$ only when $\mathbf{r}_3$ belongs to the ray passing through $\mathbf{r}_1$ and $\mathbf{r}_2$ [*Brekhovskikh and Godin*, 1999].

The compressed cross-correlation function defined by equation (26) is an integral characteristic of the wave cross correlation over the entire frequency band. When the frequency band of observations is sufficiently broad and/or wavefield properties change considerably across the band, it is desirable to preserve some frequency resolution. To this end, we introduce a set of functions, where the cross-correlation function is "compressed" in finite subbands rather than in the entire frequency band of observations. These functions will be referred to as partial compressed cross-correlation functions (PC3Fs) and are defined as follows:

$$C_{12}^{(p)}(L, \omega_0, \Delta\omega) = 2\mathrm{Re}\int_{\omega_0-\Delta\omega}^{\omega_0+\Delta\omega} H_{12}(\omega)\exp\left(i\left[\Phi(\mathbf{r}_1, \mathbf{r}_2, \omega) - \frac{\pi\gamma}{4}\right]\frac{L}{L_0}\right) d\omega. \tag{28}$$

This definition differs from the C3F definition (26) only by limits of integration. When the frequency band of observations is split into a finite number of nonoverlapping subbands, C3F equals the sum of corresponding PC3Fs. Being calculated over narrower frequency bands, PC3Fs may be less robust than C3F and require longer averaging time but, as will be demonstrated in sections 3 and 4, these provide additional insight into properties of the IGW field and the sensors used to collect the data.

In particular, it follows from equation (28) that, for sufficiently small $\Delta\omega$, the ratio of heights of PC3F peaks at $L = \pm L_0$ is equal to the ratio of the coefficients $\tilde{Q}_1$ and $\tilde{Q}_2$ in equation (17) for the cross-correlation function. The latter ratio, as shown in section 2.2, equals the ratio of the power fluxes carried by IGWs in opposite directions along the eigenray connecting points $\mathbf{r}_1$ and $\mathbf{r}_2$. Thus, calculation of PC3Fs for a number of sensor pairings allows one to characterize the directivity of the IGW field. Unlike traditional plane-wave beamforming techniques [*Van Trees*, 2004; *Webb et al.*, 1991], such an approach does not impose any limitations on wave speed (hence, bathymetry) variations in the region where the sensor array is located.

3. Observations and Data Processing

3.1. MOANA Experiment

The Marine Observations of Anisotropy Near Aotearoa (MOANA) Seismic Experiment is an ocean-bottom seismic experiment that was designed for studies of tectonic plate boundary processes through mantle

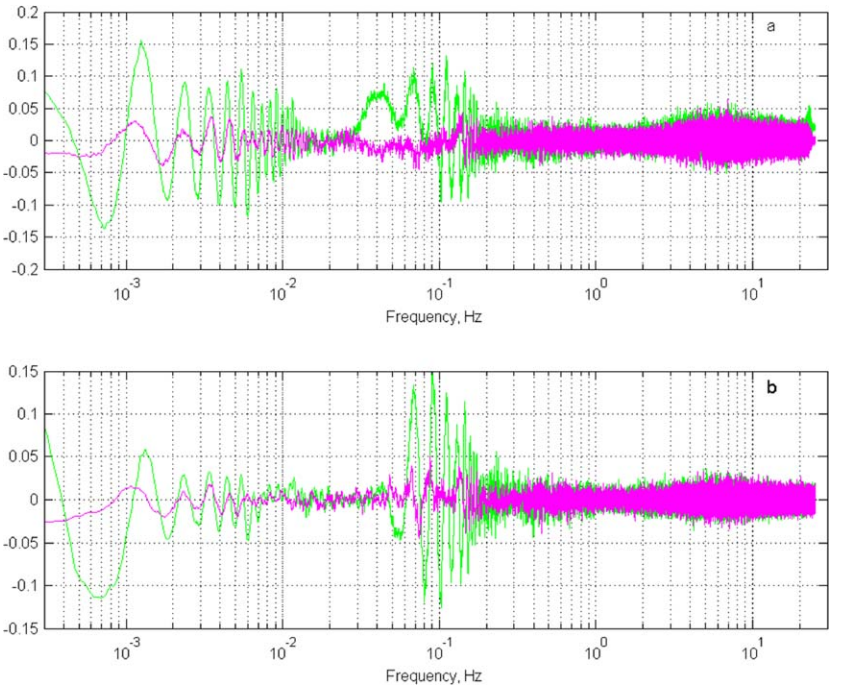

Figure 3. Real (green line) and imaginary (purple line) parts of the coherence function for stations 24 and 25 (a) before and (b) after detiding. Averaging is performed over the entire yearlong observation period.

seismic imaging. The experiment was carried out from January 2009 to February 2010 offshore the South Island of New Zealand [*Yang et al*., 2012; *Godin et al*., 2013]. A total of 30 stations was deployed east and west of the South Island at approximately 100 km spacing and at water depths from 550 to 4680 m (Figure 1). In addition to a broadband ocean bottom seismometer (OBS), each station was equipped with a Cox-Webb deep water differential pressure gauge (DPG). DPGs measure variations of pressure on the seafloor with frequencies above ∼1 mHz [*Cox et al*., 1984; *Webb et al*., 1991]. Data were recorded continuously at 50 samples per second and stored in daylong data segments.

In this study, we focus on the DPG data. Yearlong pressure records were successfully retrieved from 28 stations. The sensors were equipped with synchronized clocks. Median clock drift was 2.4 ms/day. Among the 28 stations, maximum and minimum clock drifts were −11.8 ms/day and −0.2 ms/day, resulting in clock drifts of −4.26 s and −0.06 s, respectively, over the 1 year deployment. The clock drift was corrected for in the data, resulting in clock accuracy that was more than sufficient for yearlong studies of the wave activities with periods exceeding 30 s. Pressure sensors were not individually calibrated and were instead characterized by a nominal (average) transfer function. The variations in the laboratory-measured sensitivities and corner frequencies of 10 DPGs, of identical design to those used in the MOANA array, were found to be 10% and 25%, respectively [*Godin et al*., 2013]. As discussed in section 3.2 below, our data processing approach is insensitive to amplitude distortions. Moreover, the compressed cross-correlation function technique allows us to identify and remove the systematic phase differences between the sensors, which stem from deviations of the actual transfer functions from the nominal one.

3.2. Processing

Tidal signals are dominant in seafloor pressure variations, and preventing spectral aliasing of the tidal energy is crucial. Noise interferometry relies on accurate measurements of the relatively small coherence between measurements by spatially separated sensors. The requirements to aliasing suppression are particularly stringent in noise interferometry, since, being a time-periodic process with a rather large spatial scale, the tides contribute disproportionately strongly into the coherence (Figure 3). To avoid the aliasing, we have used segments with a length equal to the period $T_{M2} \approx 12.42$ h of the dominant tidal component, lunar tide M2. The segment's lengths expressed in counts was equal to 2,235,600. The Hann window [*Dahlen*, 1982] was applied to the data segments to suppress any influence of the other tidal components.

As confirmed by computer simulations, the combination of these two simple steps reduced the contributions of parasitic harmonics of the tides by ~15 orders of magnitude in the IGW frequency band, thus making more sophisticated, model-based detiding procedures unnecessary for our purposes. In addition to possible aliasing of tidal energy into IGW frequency band, there exists a real process of IGW energy modulation by tides [*Henderson et al*., 2006; *Thomson et al*., 2006; *Guedes et al*., 2013] due to tidal changes in the littoral zone where the IGWs are generated. It should be emphasized that our simple detiding procedure suppresses aliasing of the tidal energy without affecting tidally modulated IGW energy as long as the sensors (in our case, DPGs) and the deep water IGW field remain linear.

Each daylong recording produced three overlapping data segments, each of T_{M2} duration. The segments were chosen at the beginning, middle, and end of the recording, respectively. To separate the background (ambient) IGWs from waves generated by earthquakes, tsunamis, and explosive degassing of the sediments, the data segments were automatically screened for the presence of strong, transient events. The increased average amplitude of the spectrum within the "noise notch" [*Webb et al*., 1991; *Webb and Crawford*, 2010] that is normally present in the power spectral densities of the seafloor pressure variations between the infragravity wave band and the microseism band was used as the screening criterion [*Godin et al*., 2013]. Five percent of the recordings for every station with the highest level of spectral harmonics at the frequency interval 50–60 mHz were excluded from our analysis.

The coherence function $H_{12}(\omega)$ is calculated as an average over a large number of data segments, typically, over the entire yearlong observation period. A typical example of the coherence function is shown in Figure 3. Note significant distortion of the actual coherence function (Figure 3b) by tidal energy aliasing (Figure 3a). The sensors were split in two groups; 1–21 to the west and 22–30 to the east of the South Island (Figure 1). Coherence functions were calculated for all possible pairings of sensors within each group. For all the sensor pairs, the data show elevated coherence levels in three frequency bands, which are associated with IGWs (below ~30 mHz), microseisms (around 0.05–0.9 Hz), and acoustic waves (above ~3 Hz) (Figure 3b).

In this paper, we focus on infragravity waves and choose the spectral interval $f_{\min} \le f \le f_{\max}$ with $f_{\min} = 0.5$ mHz and $f_{\max} = 30$ mHz. All frequency content of the coherence function outside this band was filtered out. The shape of the filtering window provided smooth tapering at its boundaries. The choice of the lower-frequency bound, $f_{\min}$, is due to the intrinsic limitations of the sensors; DPGs are not expected to provide reliable in situ pressure measurements at frequencies below 0.5 mHz [*Cox et al*., 1984].

When evaluating the two-point cross-correlation function of measured seafloor pressure fluctuations, we applied the power spectrum prewhitening procedure, which is described in section 2.3. Then, the cross-correlation function is given by a Fourier transform of the coherence function.

Calculation of the compressed cross-correlation function (C3F) (26) and the partial compressed cross-correlation function (PC3F) (28) from the coherence function requires knowledge of sensor horizontal separation L_0, which we calculate as the distance along the great circle path, and the eikonal Φ (11). While the exact value of the eikonal is given by an integral over the frequency-dependent eigenray connecting the locations $\mathbf{r}_1$ and $\mathbf{r}_2$ of the sensors, integration of the wave number $k(\mathbf{r}, \omega)$ over the great circle path between $\mathbf{r}_1$ and $\mathbf{r}_2$ gives the eikonal with accuracy up to terms of the second order in the cross-range gradients of environmental parameters [*Godin*, 2002]. Other than the applicability of the ray theory itself, in this approximation there are no restrictions on the rate of the environmental parameter variation in the $\mathbf{r}_1 - \mathbf{r}_2$ direction.

In C3F and PC3F calculations, we used the IGW dispersion relation (4), where the only environmental parameter is the ocean depth $H(\mathbf{r})$. The bathymetry for our calculations was taken from the ETOPO1, a 1 arc-minute global relief model of the Earth's surface [*Amante and Eakins*, 2009]. By evaluating explicit expressions [*Godin*, 2002] for the second-order eikonal corrections in the cross-range bathymetry gradients $\nabla H - \nabla H \cdot (\mathbf{r}_1 - \mathbf{r}_2)|\mathbf{r}_1 - \mathbf{r}_2|^{-1}$, and by comparing the great-circle-path integral to "exact" calculations involving numerical ray tracing, the first-order approximation was found to be sufficiently accurate. Technically, the $\Phi(\mathbf{r}_1, \mathbf{r}_2, \omega)$ values were precalculated for every pair of stations and for every frequency appearing in the discrete spectra of the pressure variations.

For PC3F calculations, we divided the frequency band $f_{\min} \le f \le f_{\max}$ into 32 intervals of equal width. Then, PC3F is a function of two arguments: L and the central frequency ω_0 of every interval. A typical example of PC3F is presented in Figure 4. The positions of various elements of PC3F (28) with relation to the expected

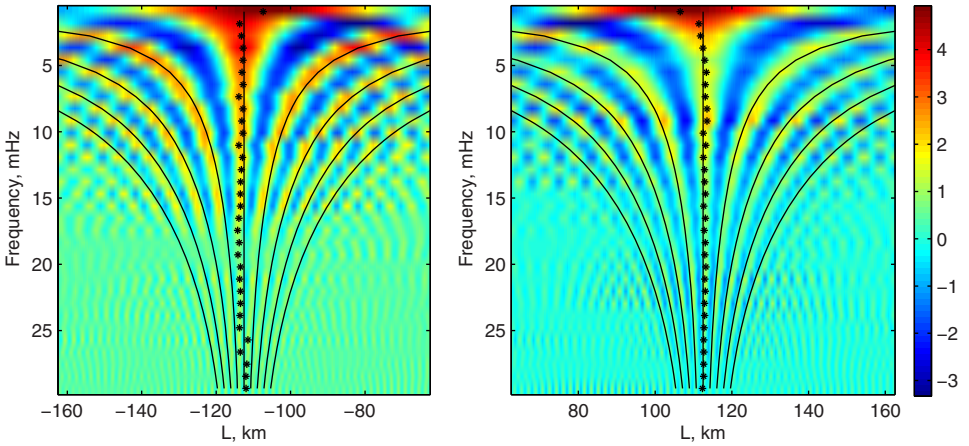

Figure 4. Partial compressed cross-correlation function (PC3F) for stations 23–30 averaged over approximately a year of pressure variation records. PC3F is defined by equation (28) and is shown by color as a function of frequency and the distance *L*, which is the counterpart of the time lag in the conventional cross-correlation function. PC3F is arbitrarily normalized. Black vertical straight lines show expected positions of the main peaks corresponding to the distance between the two stations. The asterisks mark actual positions of the main peaks. Shifts in positions may be expressed in phase units, and the black curves mark positions corresponding to the phase shifts equal to an integer number (from 1 to 4) of 2π. Positions of the secondary PC3F peaks are close to these lines.

position of the main peak at $L = L_0$ or $L = -L_0$, ΔL, can be expressed in radians ($\Delta\Phi$) through the relation $\left[\Phi(\mathbf{r}_1, \mathbf{r}_2, \omega_0) - \frac{\pi\gamma}{4}\right]\frac{L}{L_0} = \Delta\Phi$. For narrow-band compression, PC3F has additional peaks (sidelobes), which align along the hyperbola-like curves defined by the equation $\Delta\Phi = 2\pi N, N = \pm 1, \pm 2, \ldots$ (Figure 4).

The asymmetry in the shifts of the main peaks with relation to their expected symmetric positions $L = \pm L_0$ is of particular significance. Three mechanisms can contribute to the asymmetry. First, the peaks are asymmetrical in the case of nonreciprocal wave propagation, where the eikonals are different for waves propagating in opposite directions between points $\mathbf{r}_1$ and $\mathbf{r}_2$. IGW nonreciprocity can be caused by Earth rotation and oceanic currents. Nonreciprocity due to Earth's rotation is negligible for free IGWs in the frequency range we consider [*Gill*, 1982]. For current-induced nonreciprocity, $|\Delta\Phi| \sim ku|\Delta\Phi|/\omega$, where u is the depth-averaged and range-averaged current speed and is much smaller than unity in the MOANA experiment.

Second, the asymmetry of the peaks can result from the wavefield being anisotropic, i.e., having a nonuniform angular spectrum. However, the corresponding $\Delta\Phi$ value is small compared to unity as long as $kL_0 >> 1$ [*Godin*, 2009c; *Froment et al.*, 2010]. Third, if transfer functions of two pressure sensors have different phases, then the measured coherence function differs from the coherence function of the seafloor pressure by the factor $\exp[i\alpha(\omega)]$, where $\alpha(\omega)$ is the difference of phases of the transfer functions of sensors 1 and 2.

The PC3Fs of the experimental data were found to have relatively small but significant, frequency-dependent asymmetry of the main peaks. We attribute the asymmetry to individual DPGs having distinct transfer functions and use the peaks locations to measure the phase shift between the sensors, which is subsequently used to correct the phase of the coherence function. The required phase correction of the coherence function is calculated as a function of the central frequency ω_i of every frequency interval from the positions $L_L(\omega_i)$ and $L_R(\omega_i)$ of the PC3F main left and right peaks using the following equation:

$$\alpha(\omega_i) = \left[\Phi(\mathbf{r}_1, \mathbf{r}_2, \omega_i) - \frac{\pi\gamma}{4}\right]\frac{L_L(\omega_i) + L_R(\omega_i)}{2L_0}. \tag{29}$$

The correction is applied by introducing the calibration factor $\exp[-i\alpha(\omega)]$ in the integrands of equations (26) and (28). Spline interpolation helps to fill in all the values of the function $\alpha(\omega)$. Then, the second iteration is performed and new C3F and PC3F functions are obtained. The calibration procedure does not change significantly the amplitudes of the main peaks of these functions, but does correct their positions. Usually, one iteration is sufficient, but if necessary the number of iterations may be increased.

The phase correction has a pronounced effect on the fine structure of the coherence function, as illustrated by Figure 5. The seafloor pressure coherence functions obtained after the sensor calibration procedure

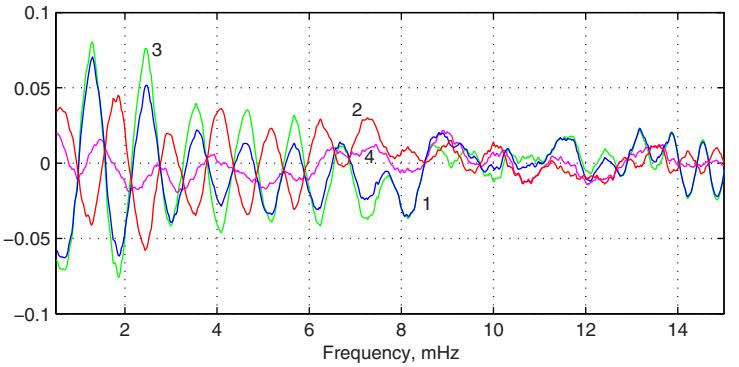

Figure 5. Real and imaginary parts of the coherence function for stations 22–23 before and after the first round of the transfer function calibration procedure. Real and imaginary parts of the coherence function are shown, respectively, by lines 1 and 2 before and by lines 3 and 4 after the calibration.

become consistent with the results of the asymptotic theory (see equations (14) and (17)), which predicts a $\pi/2$ phase shift between the real and imaginary parts of the coherence function of diffuse IGW fields.

4. Experimental Results

Calculation of coherence and cross-correlation functions of seafloor pressure fluctuations measured by different MOANA sensors demonstrated significant levels of coherence in agreement with the theory of diffuse noise fields (section 2.2), provided both sensors were located either to the east or to the west of the South Island. The island is a barrier to IGW propagation, and no coherence in the IGW frequency band was found between measurements made by sensors in the east and the west groups. Figure 6 shows several examples of the cross-correlation function. The largest peaks at the positive and the negative time lags are due to the low-frequency end of the frequency band, where IGWs become essentially nondispersive. The positions of these peaks correspond to IGW propagation with group velocity $c_g = [gH(\mathbf{r})]^{1/2}$. The other peaks, which form a shape with a triangular envelope at longer positive and negative time lags, are, on the contrary, entirely due to the strong dispersion of the higher-frequency components of the spectrum. Similar shapes can be seen in IGW cross-correlations measured in the Indian Ocean off Sumatra [*Harmon et al.*, 2012]. The decrease in the peak amplitude with increasing absolute value of the lag is solely due to IGW dispersion and is not related to the IGW power spectrum.

The shape of the cross-correlation functions makes it difficult to accurately retrieve quantitative information about IGWs. Spreading of the IGW energy across a wide range of time lags decreases signal-to-noise ratio and, therefore, rather long averaging times are required for deterministic features to emerge from the random background. The compressed cross-correlation function approach (section 2.3) allows for the energy that is otherwise distributed in time to sum up constructively (Figure 2). Instead of broad triangular shapes, the deterministic features in the C3Fs of seafloor pressure fluctuations are represented by narrow peaks around $\pm L_0$, where L_0 is the horizontal separation of the sensors (Figure 2). As illustrated by Figure 2, experimentally obtained C3Fs are rather close to theoretically predicted ones. The C3F shape is well suited for measurements of the peaks' positions, which contain kinematic information regarding the IGW propagation, and their heights, which are proportional to the IGW power flux along the ray connecting the sensors, see section 2.2.

The data accumulation time necessary to reveal peaks of C3F is relatively short; for most pairings of the MOANA stations, a few days were usually sufficient. Using the C3F technique, we were able to quantify cross correlations of the seafloor pressure for all available sensor pairings (Figure 7a), including the maximum range of 692 km (Figure 7b). To our knowledge, this is by far the longest distance at which correlation of diffuse wavefields in the ocean has been observed with pressure sensors.

As expected (section 2.2), the height of the C3F peaks lessens with increasing sensor separation, decreasing the contrast between the deterministic features and noise. Eikonal calculation errors, which are caused by uncertainty in bathymetry and are also due to application of the first-order approximation described in section 3.2, accumulate with range. In addition to the smaller signal-to-noise ratio, these errors may contribute to decrease in the contrast. Still, the main peaks of the C3F occur at the predicted positions $L = \pm L_0$ even at the largest sensor separation (Figure 7b). Note three additional C3F peaks at $L > L_0$ with a shape similar to the main peak at $L = L_0$ (Figure 7b). These satellite peaks are likely to represent IGW multipaths, i.e., existence of several frequency-dependent paths (eigenrays) connecting the sensors. This is consistent with

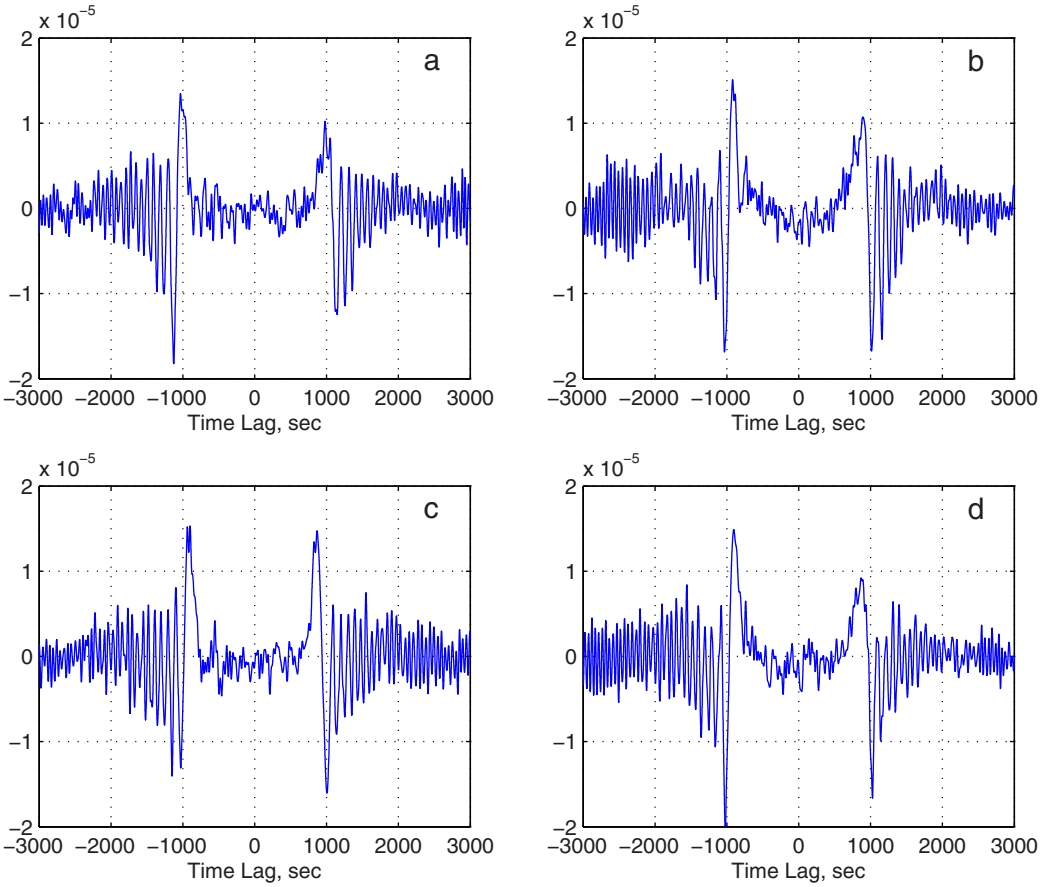

Figure 6. Examples of conventional cross-correlation function of pressure variations from the year-averaged data of MOANA experiment: stations (a) 23–30, (b) 24–25, (c) 25–30, and (d) 26–27.

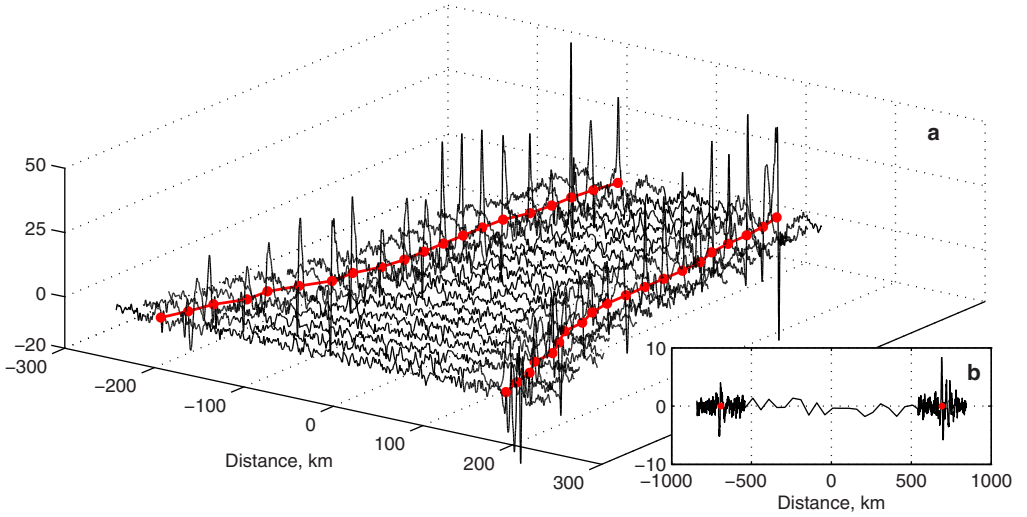

Figure 7. Compressed cross-correlation functions, or C3Fs, of seafloor pressure fluctuations in the IGW frequency band. (a) A sequence of C3Fs obtained from the data of the MOANA experiment, ordered by the distance between the stations (black lines) plotted against $\pm L_0$ (red lines). (b) C3F obtained at the largest horizontal separation of $L_0 = 692$ km between MOANA stations 1 and 21. Red dots show points $\pm L_0$. All C3Fs have common but otherwise arbitrary normalization.

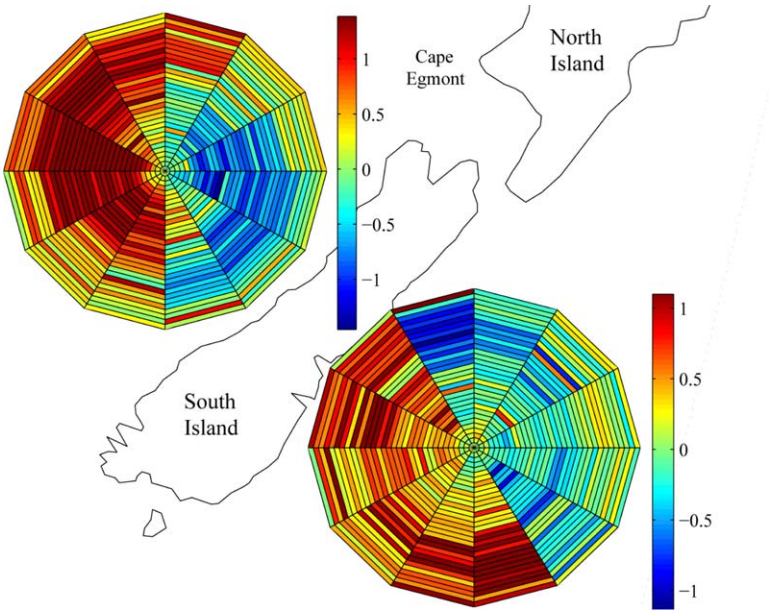

Figure 8. Time-averaged anisotropy versus frequency diagrams of the IGW field to the east and to the west of the South Island of New Zealand. Frequency varies with the radius between 0.5 mHz at the center of the circle to 30 mHz at the outer part of the circle in 32 steps. The color shows common logarithm of anisotropy in each of the 768 frequency and azimuthal direction bins, which are represented by individual trapezoids in the figure. The anisotropy is defined as the ratio of net IGW power fluxes in the given azimuthal direction and in the opposite direction.

accurate ray calculations (as opposed to simplified calculations described in section 3.2) for stations 1 and 21.

Except for the longest ranges, the positions of the C3F peaks coincide with the expected value $L = \pm L_0$ with accuracy $O(1)$ km, often within a fraction of the water depths at the sensor locations. This is close to the diffraction limit of accuracy, since the water depth sets the scale for the shortest IGWs that contribute appreciably to the seafloor pressure fluctuations (see equation (3)). It should be emphasized that neither such an accuracy of the peak positions nor quality of the cross-correlation function compression (as quantified by the peaks' heights) can be achieved without accounting for the actual bathymetry variation between the sensors. The appearance of the main C3F peaks at $L = \pm L_0$ (Figure 7a) proves that the free surface gravity waves—as opposed to coastally trapped waves such as Kelvin waves [*LeBlond and Mysak*, 1978; *Gill*, 1982]—are responsible for the observed pressure fluctuations, and the dispersion equation of these free waves is closely approximated by the dispersion equation (4) implied in the compression algorithm (26). This is consistent with earlier studies at other deep water sites [*Webb*, 1986, 1998; *Webb et al*., 1991]. Moreover, the absence at $L < |L_0|$ of C3F peaks with heights comparable to the main peaks for sensor pairs with various azimuthal orientation, proves that the IGW field is diffuse and there are no compact IGW sources appreciably contributing to the observed ambient IGW field.

These findings, which have been derived from C3Fs of the data, can be further confirmed using PC3Fs (Figure 4). Analysis of the positions of the PC3F peaks for various sensor pairs confirms the validity of the above conclusions, that free IGWs are responsible for the observed seafloor pressure fluctuations and that the IGW field is diffuse, in each subband in the frequency band $f_{\min} \le f \le f_{\max}$.

We have established analytically (sections 2.2 and 2.3) and verified by numerical simulation that the directivity (angular spectrum) of IGWs in the horizontal plane can be obtained from measurements of the heights of the peaks of PC3Fs at $L = \pm L_0$. We use the groups of sensors to the east and west of the South Island as arrays to measure anisotropy of IGW fields in the respective basins. The theory of sections 2.2 and 2.3 applies to cross correlations calculated within each group of sensors because IGWs experience neither considerable scattering (as opposed to refraction) nor attenuation [*Van Dorn*, 1984, 1987; *Geist et al*., 2009; *Rabinovich et al*., 2013], when propagating between sensors in the same group. We divide a complete circle around the nominal geometrical center of each group into 12 sectors 30° wide each. Following equation (24), we calculate the ratios of the amplitudes of the two main peaks of the PC3F (multiplied by the respective wave numbers) for every pair of the stations and for each of 32 central frequencies and attribute it to the absolute azimuth of the line connecting the two stations. The reciprocal value, i.e., the multiplicative inverse quantity, is attributed to the opposite direction, i.e., the original azimuth plus 180°. Then, we average all the values that get into each of the 12×32 small trapezoids and represent the result using a color scale in a near-circular diagram (see Figure 8). What is obtained is a set of 32 rings, each resembling the

wind rose; only the relative intensity of the IGW field is shown by color, not by radius length. The closer the color to red, the more energy propagates in this direction at this particular frequency. Blue colors represent energy propagating away from a given direction, and green represents isotropic propagation. Our measurements of IGW anisotropy are much more detailed than previously published results [*Webb et al*., 1991; *Harmon et al*., 2012] for other deep water sites.

The anisotropy versus frequency diagrams (Figure 8) obtained for basins to the east and to the west of the New Zealand's South Island have some common properties. They both tell us that the lowest-frequency components of the IGW spectrum (plotted toward the center of the circle) are largely isotropic (green colors). The anisotropy has its maximum in the middle of the IGW spectral band (strongest reds and blues) and falls back to insignificant levels (greens and yellows) at the high-frequency end of the spectrum.

Complex nonlinear processes of wave interaction with tides and bathymetry take place near coastline, leading to both generation of IGWs by higher-frequency wind waves and swell and to partial absorption of the incoming IGW energy [*Henderson et al*., 2006; *Thomson et al*., 2006; *Guedes et al*., 2013]. Both anisotropy diagrams in Figure 8 have their highest peaks for the waves coming from the New Zealand coasts, which is consistent with the common notion of the coastal origin of IGWs [*Foda and Mei*, 1981; *Symonds et al*., 1982; *Herbers et al*., 1995]. However, there is a notable difference between the general orientations of the two diagrams: the eastern one displays a significant contribution from the waves propagating along the coastline in the general southwest direction and probably coming from powerful sources in the northeastern Pacific [*Aucan and Ardhuin*, 2013], to which this group of stations is exposed, while the western group of sensors is largely shielded from the northeastern Pacific sources by New Zealand's North Island. Red colors in the western sectors of the eastern anisotropy diagram indicate that parts of the southeast coast of the South Island prove to be net sinks of the IGW energy.

In the western group of stations, the anisotropy maximum corresponds largely to IGWs coming from the vicinity of New Zealand's stormy Cape Egmont (Figure 1). Location of the blue colors in the western anisotropy diagram clearly shows that there is a rather strong anisotropy between IGWs propagating to and from the South island in the Tasman Sea. IGW power flux from the coast can exceed the power flux toward the coast by a factor of 10 or more (Figure 8). Thus, the northwest coast of the South Island is a net source of the IGW energy.

5. Discussion

We have demonstrated that the two-point cross-correlation function of IGWs can be measured at distances as large as 700 km in the ocean. Since the cross-correlation function approximates the deterministic Green's function, such measurements of the background IGWs provide what can be called "tsunamis on demand" and can be used to experimentally verify numerical models of tsunami propagation. With the wave interferometry approach, tsunami surrogates can be obtained from observations of background IGWs for any pair of points of interest and without requiring that IGWs are generated in a localized region. Because of their larger wavelength, it is likely that correlation measurements of very low frequency IGWs, which are of primary interest to tsunami research and modeling, will be successful at ranges up to thousands of kilometers. However, absolute pressure sensors may be required to go beyond the low-frequency limitations of DPGs.

Our compressed cross-correlation function, or C3F, technique is fundamentally based on the theoretical result that the two-point cross-correlation function of a directional, diffuse wavefield in an inhomogeneous medium is kinematically equivalent to the sum of deterministic Green's functions that describe wave propagation in opposite directions between the two points [*Godin*, 2006, 2010], see equations (17) and (18). The equivalence suggests application to the cross-correlation function of the signal processing methods originally developed for deterministic wavefields. In particular, the C3F technique bears similarity to well-known wavefront reversal and back propagation [*Tappert et al*., 1985; *Fink*, 1996; *Anderson et al*., 2013] and mode separation [*Xu et al*., 2012] methods normally applied to deterministic wavefields.

By calculating the eikonal Φ in equation (26) using the dispersion equations of various known wave types, the C3F technique can be used to identify the contributions of respective waves into the observed pressure fluctuations. We have considered several conceivable contributors, such as various coastally trapped ocean waves [*LeBlond and Mysak*, 1978; *Gill*, 1982] and atmospheric Lamb waves over the ocean surface [*Godin*

and Fuks, 2012]. However, no evidence was found of measurable contributions of any waves other than free IGWs into the observed seafloor pressure fluctuations in the frequency band of our study.

Useful applications of the C3F technique to IGW research are not limited to those demonstrated in this work. Below, we briefly outline two additional, promising ways to extract valuable information about IGWs and their propagation environment from seafloor pressure data, which will be the subject of our future work.

IGW amplitude on the seafloor exponentially decreases with increasing kH and, at relatively high frequencies or large water depths H, becomes small compared to pressure fluctuations due to ocean currents and other processes. This is often referred to as hydrodynamic filtering [*Webb et al*., 1991]. Hydrodynamic filtering restricts the frequency band, where IGW power spectra can be retrieved from single-point measurements using sensors on the seafloor [e.g., *Webb*, 1988; *Dolenc et al*., 2005, 2008; *Sugioka et al*., 2010; *Yang et al*., 2012; *Godin et al*., 2013], and limits the vertical resolution of the ocean bottom inversions based on the seafloor compliance measurements [*Crawford*, 2004; *Crawford and Singh*, 2008; *Crawford et al*., 1991, 1998; *Trevorrow and Yamamoto*, 1991; *Wang et al*., 2010; *Willoughby and Edwards*, 2000; *Willoughby et al*., 2008]. In PC3Fs, we are able to trace IGW contributions to considerably higher frequencies than in respective single-point measurements. This is not surprising since the contributions of the flow and instrument noise into the cross correlation of measurements by spatially separated sensors are much smaller than into the pressure variance at each point. Application of the compression (26) to the cross spectrum, rather than the coherence function, of the seafloor pressure measurements is expected to provide a way to characterize the IGW-induced pressure fluctuations in a wider frequency band than is possible with single-point measurements. Similarly, application of the compression (26) to the cross spectrum of the vertical displacements measured by spatially separated ocean bottom seismometers is expected to improve characterization of the IGW-induced deformations of the seafloor.

The quality of the cross-correlation function compression and positions of the C3F main peaks depend on the accuracy of modeling the eikonal Φ in equation (26). Much like the positions of nulls of the cross-correlation function of nondispersive acoustic noise serve as input information for retrieval of the sound-speed profile in passive ocean acoustic tomography [*Godin et al*., 2010], frequency-dependent deviations of the main peaks of PC3Fs of IGWs can be used, in principle, to measure physical parameters of the ocean, such as seafloor compliance, and constrain deviations of the bathymetry from available maps. Preliminary estimates indicate that, under conditions of the MOANA experiment, seafloor compliance has a measurable effect on IGWs, which, however, needs to be separated from comparable effects due to uncertainties in bathymetry. Further research is necessary to assess the feasibility of tomographic measurements of seafloor compliance based on IGW interferometry.

6. Conclusions

Long-term, multistatic observations of seafloor pressure provide a wealth of quantitative information about infragravity waves and help fill the gaps in the available knowledge of IGW properties away from shore. Using DPG measurements of seafloor pressure off New Zealand, we have demonstrated that ambient IGWs retain significant, measurable coherence at ranges of 700 km. This observation suggests application of noise interferometry techniques [*Rickett and Claerbout*, 1999; *Shapiro et al*., 2005; *Wapenaar et al*., 2008; *Godin et al*., 2010] to remote sensing of IGWs on basin scales.

We have found that, in the Tasman Sea and in the southwestern Pacific off the South Island of New Zealand, free surface gravity waves, as opposed to coastally trapped waves [*LeBlond and Mysak*, 1978; *Gill*, 1982], dominate in the ambient IGW field. The field is diffuse in the sense that IGWs come from all horizontal directions, albeit with time-averaged power flux being strongly azimuthally anisotropic. In contrast to transient events such as due to earthquakes or volcanic eruptions, no evidence was found for compact wave sources contributing significantly into the background (ambient) IGW field. These conclusions are restricted to water depths over 550 m by the placement of seafloor pressure sensors used in this study.

We have measured IGW anisotropy with high angular and frequency resolution. This was made possible by a new interferometric approach, dubbed the compressed cross-correlation function technique, which compensates for wave packets' spreading due to wave dispersion and rigorously relates the magnitude of

maxima in the wave cross correlations to the anisotropy of the power flux carried by the waves. Unlike traditional plane-wave beamforming approaches, the new technique is not restricted to basins with negligible bathymetry variations. While IGW power spectra are essentially the same to the east and to the west of the South Island [*Yang et al*., 2012; *Godin et al*., 2013], IGW directivity proves to be rather different in the respective basins. Specific IGW generation sites responsible for the observed anisotropy peaks have been suggested. Our anisotropy measurements provide input information for future investigations of deep water IGW generation on and scattering from the continental shelf.

In addition to measurements of the IGW directivity, the compressed cross-correlation function technique proposed in this paper offers a number of additional avenues for investigation of IGWs in the ocean as well as for studies of diffuse, random fields of other dispersive waves and their respective propagation media.

Acknowledgments

The collection of DPG data was supported by the National Science Foundation Continental Dynamics program under grants EAR-0409564, EAR-0409609, and EAR-0409835. The instruments were provided by the U.S. National Ocean Bottom Seismic Instrumentation Pool (http://www.obsip.org). We are grateful to Zhaohui Yang for facilitating access to the MOANA experiment data set. Data processing and numerical simulations were performed on the Janus supercomputer, which is supported by the National Science Foundation (award CNS-0821794) and the University of Colorado Boulder. The Janus supercomputer is a joint effort of the University of Colorado Boulder, the University of Colorado Denver and the National Center for Atmospheric Research. This work was supported, in part, by the University of Colorado Seed Grant "Study of Ocean Infragravity Waves with a Large Array of Seafloor Seismometers," the National Science Foundation award OCE 1129524, and the Office of Naval Research award N00014-13-1–0348.

References

Amante, C., and B. W. Eakins (2009), ETOPO1 1 arc-minute global relief model: Procedures, data sources and analysis, *NOAA Tech. Memo. NESDIS NGDC-24*, 19 pp., Boulder, Colo.

Anderson, B. E., T. J. Ulrich, and P.-Y. Le Bas (2013), Comparison and visualization of focusing wave fields from various time reversal techniques in elastic media, *J. Acoust. Soc. Am.*, *134*, EL527–EL533.

Ardhuin, F., and T. H. C. Herbers (2013), Noise generation in the solid Earth, oceans and atmosphere, from nonlinear interacting surface gravity waves in finite depth, *J. Fluid Mech.*, *716*, 316–348, doi:10.1017/jfm.2012.548.

Aucan, J., and F. Ardhuin (2013), Infragravity waves in the deep ocean: An upward revision, *Geophys. Res. Lett.*, *40*, 3435–3439, doi:10.1002/grl.50321.

Brekhovskikh, L. M., and O. A. Godin (1999), *Acoustics of Layered Media. 2: Point Sources and Bounded Beams*, 2nd ed., Springer, Berlin.

Bromirski, P. D., and R. A. Stephen (2012), Response of the Ross Ice Shelf, Antarctica, to ocean gravity-wave forcing, *Ann. Glaciol.*, *53*(60), 163–172.

Bromirski, P. D., O. V. Sergienko, and D. R. MacAyeal (2010), Transoceanic infragravity waves impacting Antarctic ice shelves, *Geophys. Res. Lett.*, *37*, L02502, doi:10.1029/2009GL041488.

Campillo, M., and A. Paul (2003), Long-range correlations in the diffuse seismic coda, *Science*, *299*, 547–549.

Cox, C., T. Deaton, and S. Webb (1984), A deep-sea differential pressure gauge, *J. Atmos. Oceanic Technol.*, *1*, 237–246.

Crawford, W. C. (2004), The sensitivity of seafloor compliance measurements to sub-basalt sediments, *Geophys. J. Int.*, *157*, 1130–1145.

Crawford, W. C., and S. C. Singh (2008), Sediment shear properties from seafloor compliance measurements: Faroes-Shetland basin case study, *Geophys. Prospect.*, *56*, 313–325.

Crawford, W. C., S. C. Webb, and J. A. Hildebrand (1991), Seafloor compliance observed by long-period pressure and displacement measurements, *J. Geophys. Res.*, *96* (B10), 16, 151–116, 160.

Crawford, W. C., S. C. Webb, and J. A. Hildebrand (1998), Estimating shear velocities in the oceanic crust from compliance measurements by two-dimensional finite difference modeling, *J. Geophys. Res.*, *103* (B5), 9895–9916.

Dahlen, F. A. (1982), The effect of data windows on the estimation of free oscillation parameters, *Geophys. J. R. Astron. Soc.*, *69*, 537–549.

Dolenc, D., B. Romanowicz, D. Stakes, P. McGill, and D. Neuhauser (2005), Observations of infragravity waves at the Monterey ocean bottom broadband station (MOBB), *Geochem. Geophys. Geosyst.*, *6*, Q09002, doi:10.1029/2005GC000988.

Dolenc, D., B. Romanowicz, P. McGill, and W. Wilcock (2008), Observations of infragravity waves at the ocean-bottom broadband seismic stations Endeavour (KEBB) and Explorer (KXBB), *Geochem. Geophys. Geosyst.*, *9*, Q05007, doi:10.1029/2008GC001942.

Duvall, T. L., S. M. Jeffferies, J. W. Harvey, and M. A. Pomerantz (1993), Time-distance helioseismology, *Nature*, *362*, 430–432, doi:10.1038/362430a0.

Eckart, C. (1960), *Hydrodynamics of Oceans and Atmospheres*, Pergamon, New York.

Elgar, S., T. H. C. Herbers, M. Okihiro, J. Oltman-Shay, and R. T. Guza (1992), Observations of infragravity waves, *J. Geophys. Res.*, *97*, 15,573–15,577.

Filloux, J. H. (1983), Pressure fluctuations on the open ocean floor off the Gulf of California: Tides, earthquakes and tsunamis, *J. Phys. Oceanogr.*, *13*, 783–796.

Fink, M. (1996), Time reversal in acoustics, *Contemporary Phys.*, *37*, 95–109.

Foda, M. A., and C. C. Mei (1981), Nonlinear excitation of long-trapped waves by a group of short swells, *J. Fluid Mech.*, *111*, 319–345.

Froment, B., M. Campillo, P. Roux, P. Gouédard, A. Verdel, and R. L. Weaver (2010), Estimation of the effect of nonisotropically distributed energy on the apparent arrival time in correlations, *Geophysics*, *75*, SA85–SA93.

Galvan, D. A., A. Komjathy, M. P. Hickey, P. Stephens, J. Snively, Y. Tony Song, M. D. Butala, and A. J. Mannucci (2012), Ionospheric signatures of Tohoku-Oki tsunami of March 11, 2011: Model comparisons near the epicenter, *Radio Sci.*, *47*, RS4003, doi:10.1029/2012RS005023.

Geist, E. L., P. J. Lynett, and J. D. Chaytor (2009), Hydrodynamic modeling of tsunamis from the Currituck landslide, *Mar. Geol.*, *264*, 41–52, doi:10.1016/j.margeo.2008.09.005.

Gill, A. E. (1982), *Atmosphere-Ocean Dynamics*, Academic, New York.

Godin, O. A. (2002), A 2-D description of sound propagation in a horizontally-inhomogeneous ocean, *J. Comput. Acoust.*, *10*, 123–151, doi:10.1142/S0218396X02001425.

Godin, O. A. (2006), Recovering the acoustic Green's function from ambient noise cross-correlation in an inhomogeneous moving medium, *Phys. Rev. Lett.*, *97*, 054301–1–054301-4, doi:10.1103/PhysRevLett.97.054301.

Godin, O. A. (2009a), Retrieval of Green's functions of elastic waves from thermal fluctuations of fluid-solid systems, *J. Acoust. Soc. Am.*, *125*, 1960–1970.

Godin, O. A. (2009b), Emergence of deterministic Green's functions from noise generated by finite random sources, *Phys. Rev. E*, *80*, 066605, doi:10.1103/PhysRevE.80.066605.

Godin, O. A. (2009c), Accuracy of the deterministic travel times retrieval from cross-correlations of non-diffuse ambient noise, *J. Acoust. Soc. Am.*, *126*, EL183–EL189, doi:10.1121/1.3258064.

Godin, O. A. (2010), Cross-correlation function of acoustic fields generated by random high-frequency sources, *J. Acoust. Soc. Am.*, *128*, 600–610, doi:10.1121/1.3458815.

Godin, O. A., and I. M. Fuks (2012), Transmission of acoustic-gravity waves through gas-liquid interfaces, *J. Fluid Mech.*, *709*, 313–340, doi: 10.1017/jfm.2012.336.
Godin, O. A., N. A. Zabotin, and V. V. Goncharov (2010), Ocean tomography with acoustic daylight, *Geophys. Res. Lett.*, *37*, L13605, doi: 10.1029/2010GL043623.
Godin, O. A., N. A. Zabotin, A. F. Sheehan, Z. Yang, and J. A. Collins (2013), Power spectra of infragravity waves in a deep ocean, *Geophys. Res. Lett.*, *40*, 2159–2165, doi:10.1002/grl.50418.
Gouédard, P., et al. (2008), Cross-correlation of random fields: Mathematical approach and applications, *Geophys. Prospect.*, *56*, 375–393.
Guedes, R. M. C., K. R. Bryan, and G. Coco (2013), Observations of wave energy fluxes and swash motions on a low-sloping, dissipative beach, *J. Geophys. Res.*, *118*, 3651–3669, doi:10.1002/jgrc.20267.
Harmon, N., T. Henstock, M. Srokosz, F. Tilmann, A. Rietbrock, and P. Barton (2012), Infragravity wave source regions determined from ambient noise correlation, *Geophys. Res. Lett.*, *39*, L04604, doi:10.1029/2011GL050414.
Henderson, S. M., R. T. Guza, S. Elgar, T. H. C. Herbers, and A. J. Bowen (2006), Nonlinear generation and loss of infragravity wave energy, *J. Geophys. Res.*, *111*, C12007, doi:10.1029/2006JC003539.
Herbers, T. H. C., S. Elgar, and R. T. Guza (1995), Generation and propagation of infragravity waves, *J. Geophys. Res.*, *100*, 24,863–24,872.
Keller, J. B. (1958), Surface waves on water of non-uniform depth, *J. Fluid Mech.*, *4*, 607–614.
Lani, S. W., K. G. Sabra, W. S. Hodgkiss, W. A. Kuperman, and P. Roux (2013), Coherent processing of shipping noise for ocean monitoring, *J. Acoust. Soc. Am.*, *133*, EL108–EL113.
Larose, E., L. Margerin, A. Derode, B. van Tiggelen, M. Campillo, N. Shapiro, A. Paul, L. Stehly, and M. Tanter (2006), Correlation of random wavefields: An interdisciplinary review, *Geophysics*, *71*, SI11–SI21.
LeBlond, P. H., and L. A. Mysak (1978), *Waves in the Ocean*, Elsevier, Amsterdam.
Livneh, D. J., I. Seker, F. T. Djuth, and J. D. Mathews (2007), Continuous quasiperiodic thermospheric waves over Arecibo, *J. Geophys. Res.*, *112*, A07313, doi:10.1029/2006JA012225.
Lobkis, O. I., and R. L. Weaver (2001), On the emergence of the Green's function in the correlations of a diffuse field, *J. Acoust. Soc. Am.*, *110*, 3011–3017.
Makela, J. J., et al. (2011), Imaging and modeling the ionospheric airglow response over Hawaii to the tsunami generated by the Tohoku earthquake of 11 March 2011, *Geophys. Res. Lett.*, *38*, L13305, doi:10.1029/2011GL047860.
Munk, W. H. (1949), Surf beat, *Eos Trans. AGU*, *30*, 849–854.
Peltier, W. R., and C. O. Hines (1976), On the possible detection of tsunamis by a monitoring of the ionosphere, *J. Geophys. Res.*, *81*, 1995–2000.
Rabinovich, A. B., R. N. Candella, and R. E. Thomson (2013), The open ocean energy decay of three recent trans-Pacific tsunamis, *Geophys. Res. Lett.*, *40*, 3157–3162, doi:10.1002/grl.50625.
Rhie, J., and B. Romanowicz (2004), Excitation of Earth's continuous free oscillations by atmosphere-ocean-seafloor coupling, *Nature*, *431*, 552–556.
Rickett, J., and J. Claerbout (1999), Acoustic daylight imaging via spectral factorization: Helioseismology and reservoir monitoring, *Leading Edge*, *18*, 957–960.
Roux, P., W. A. Kuperman, and the NPAL Group (2004), Extracting coherent wave fronts from acoustic ambient noise in the ocean, *J. Acoust. Soc. Am.*, *116*, 1995–2003.
Rytov, S. M. (1956), On thermal agitation in distributed systems, *Sov. Phys. Dokl., Engl. Transl.*, *1*, 555–559.
Sabra, K. G., P. Roux, and W. A. Kuperman (2005), Emergence rate of the time-domain Green's function from ambient noise cross-correlation function, *J. Acoust. Soc. Am.*, *118*, 3524–3531.
Shapiro, N. M., M. Campillo, L. Stehly, and M. H. Ritzwoller (2005), High-resolution surface-wave tomography from ambient seismic noise, *Science*, *307*(5715), 1615–1618.
Shen, M. C., and J. B. Keller (1975), Uniform ray theory of surface, internal and acoustic wave propagation in a rotating ocean or atmosphere, *SIAM J. Appl. Math.*, *28*, 857–875.
Sheremet, A., R. T. Guza, S. Elgar, and T. H. C. Herbers (2002), Observations of nearshore infragravity waves: Seaward and shoreward propagating components, *J. Geophys. Res.*, *107*(C8), 3095, doi:10.1029/2001JC000970.
Snieder, R. (2004), Extracting the Green's function from the correlation of coda waves: A derivation based on stationary phase, *Phys. Rev. E*, *69*, 046610, doi:10.1103/PhysRevE.69.046610.
Snodgrass, F. E., G. W. Groves, K. F. Hasselmann, G. R. Miller, W. H. Munk, and W. H. Powers (1966), Propagation of ocean swell across the Pacific, *Philos. Trans. R. Soc. London A*, *259*(1103), 431–497.
Squire, V. A., G. L. Vaughan, and L. G. Bennetts (2009), Ocean surface wave evolvement in the Arctic Basin, *Geophys. Res. Lett.*, *36*, L22502, doi:10.1029/2009GL040676.
Sugioka, H., Y. Fukao, and T. Kanzawa (2010), Evidence for infragravity wave-tide resonance in deep oceans, *Nat. Commun.*, *1*, 84, doi: 10.1038/ncomms1083.
Symonds, G., D. A. Huntley, and A. J. Bowen (1982), Two-dimensional surf beat: Long wave generation by a time-varying breakpoint, *J. Geophys. Res.*, *87*, 492–498.
Tanimoto, T. (2005), The oceanic excitation hypothesis for the continuous oscillations of the Earth, *Geophys. J. Int.*, *160*, 276–288.
Tappert, F. D., L. Nghiem-Phu, and S. C. Daubin (1985), Source localization using the PE method, *J. Acoust. Soc. Am.*, *78*, S30.
Thomson, J., S. Elgar, B. Raubenheimer, T. H. C. Herbers, and R. T. Guza (2006), Tidal modulation of infragravity waves via nonlinear energy-losses in the surf zone, *Geophys. Res. Lett.*, *33*, L05601, doi:10.1029/2005GL025514.
Thomson, J., S. Elgar, T. H. C. Herbers, B. Raubenheimer, and R. T. Guza (2007), Refraction and reflection of infragravity waves near submarine canyons, *J. Geophys. Res.*, *112*, C10009, doi:10.1029/2007JC004227.
Trevorrow, M. V., and T. Yamamoto (1991), Summary of marine sedimentary shear modulus and acoustic speed profile results using a gravity wave inversion technique, *J. Acoust. Soc. Am.*, *90*, 441–456.
Van Dorn, W. G. (1984), Some tsunami characteristics deducible from tide records, *J. Phys. Oceanogr.*, *14*, 353–363.
Van Dorn, W. G. (1987), Tide gage response to tsunamis. Part II: Other oceans and smaller seas, *J. Phys. Oceanogr.*, *17*, 1507–1516.
Van Trees, H. L. (2004), *Detection, Estimation, and Modulation Theory. Optimum Array Processing*, John Wiley, New York.
Wadhams, P., and M. J. Doble (2009), Sea ice thickness measurement using episodic infragravity waves from distant storms, *Cold Reg. Sci. Technol.*, *56*(2–3), 98–101.
Wang, J.-H., W.-C. Chi, R. N. Edwards, and E. C. Willoughby (2010), Effects of sea states on seafloor compliance studies, *Mar. Geophys. Res.*, *31*, 99–107, doi:10.1007/s11001-010-9091-z.

Wapenaar, K., and J. Thorbecke (2013), On the retrieval of the directional scattering matrix from directional noise, *SIAM J. Imaging Sci.*, *6*, 322–340.
Wapenaar, K., D. Draganov, and J. O. A. Robertsson (Eds.) (2008), Seismic interferometry: History and present status, *SEG Geophys. Reprint Ser. 26*, Soc. of Explor. Geophys., Tulsa, Okla.
Weaver, R. L., and O. I. Lobkis (2001), Ultrasonics without a source: Thermal fluctuation correlations at MHz frequencies, *Phys. Rev. Lett.*, *87*, 134301, doi:10.1103/PhysRevLett.87.134301.
Weaver, R. L., and O. I. Lobkis (2005), Fluctuations in diffuse field-field correlations and the emergence of the Green's function in open systems, *J. Acoust. Soc. Am.*, *117*, 3432–3439.
Webb, S. C. (1986), Coherent pressure fluctuations observed at two sites on the deep sea floor, *Geophys. Res. Lett.*, *13*, 141–144.
Webb, S. C. (1988), Long-period acoustic and seismic measurements and ocean floor currents, *IEEE J. Oceanic Eng.*, *13*, 263–270.
Webb, S. C. (1998), Broadband seismology and noise under the ocean, *Rev. Geophys.*, *36*, 105–142.
Webb, S. C., and W. Crawford (2010), Shallow-water broadband OBS seismology, *Bull. Seismol. Soc. Am.*, *96*, 2723–2736.
Webb, S. C., X. Zhang, and W. Crawford (1991), Infragravity waves in the deep ocean, *J. Geophys. Res.*, *96*, 2723–2736.
Weinberg, H., and R. Burridge (1974), Horizontal ray theory for ocean acoustics, *J. Acoust. Soc. Am.*, *55*, 63–79.
Willoughby, E. C., and R. N. Edwards (2000), Shear velocities in Cascadia from seafloor compliance measurements, *Geophys. Res. Lett.*, *27*, 1021–1024.
Willoughby, E. C., K. Latychev, R. N. Edwards, K. Schwalenberg, and R. D. Hyndman (2008), Seafloor compliance imaging of marine gas hydrate deposits and cold vent structures, *J. Geophys. Res.*, *113*, B07107, doi:10.1029/2005JB004136.
Xu, K., D. Ta, P. Moilanen, and W. Wang (2012), Mode separation of Lamb waves based on dispersion compensation method, *J. Acoust. Soc. Am.*, *131*, 2714–2722.
Yang, Z., A. Sheehan, J. A. Collins, and G. Laske (2012), The character of seafloor ambient noise recorded offshore New Zealand: Results from the MOANA ocean bottom seismic experiment, *Geochem. Geophys. Geosyst.*, *13*, Q10011, doi:10.1029/2012GC004201.
Zabotin, N. A., and O. A. Godin (2011), Emergence of acoustic Green's functions from time averages of ambient noise, *Acta Acust. United Acust.*, *97*, 44–53, doi:10.3813/AAA.918385.